Dynamic Coarse-to-Fine Learning for Oriented Tiny Object Detection

Chang Xu[1], Jian Ding[2], Jinwang Wang[1], Wen Yang[1]*, Huai Yu[1], Lei Yu[1]*, Gui-Song Xia[2]

[1] School of Electronic Information, Wuhan University

[2] School of Computer Science, Wuhan University

{xuchangeis,jian.ding,jwwangchn,yangwen,yuhuai,ly.wd,guisong.xia}@whu.edu.cn

Abstract

Detecting arbitrarily oriented tiny objects poses intense challenges to existing detectors, especially for label assignment. Despite the exploration of adaptive label assignment in recent oriented object detectors, the extreme geometry shape and limited feature of oriented tiny objects still induce severe mismatch and imbalance issues. Specifically, the position prior, positive sample feature, and instance are mismatched, and the learning of extreme-shaped objects is biased and unbalanced due to little proper feature supervision. To tackle these issues, we propose a dynamic prior along with the coarse-to-fine assigner, dubbed DCFL. For one thing, we model the prior, label assignment, and object representation all in a dynamic manner to alleviate the mismatch issue. For another, we leverage the coarse prior matching and finer posterior constraint to dynamically assign labels, providing appropriate and relatively balanced supervision for diverse instances. Extensive experiments on six datasets show substantial improvements to the baseline. Notably, we obtain the state-of-the-art performance for one-stage detectors on the DOTA-v1.5, DOTA-v2.0, and DIOR-R datasets under single-scale training and testing. Codes are available at https://github.com/Chasel-Tsui/mmrotate-dcfl.

1. Introduction

The oriented bounding box is a finer representation for object detection since the object's background region is greatly eradicated by introducing the rotation angle [55]. This advantage is pronounced in aerial images, where objects are in arbitrary orientations, resulting in the prosperity of corresponding object detection datasets [7, 11, 35, 55] and customized oriented object detectors [10, 17, 18, 60, 62]. Nevertheless, one unignorable fact is that there exist numerous tiny objects in aerial images. When oriented objects are tiny-sized, the challenges posed to existing object detec-
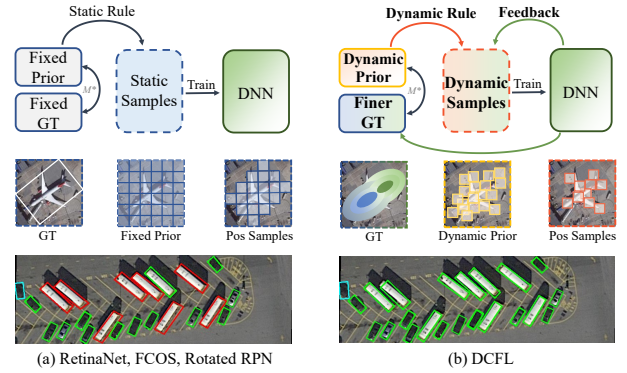
*Corresponding Authors

Figure 1. Comparisons of different learning paradigms for oriented object detection. M* means the matching function. Each box in the 2nd row denotes a prior location. The 3rd row are predictions of the RetinaNet and DCFL, where green, blue, and red boxes denote true positive, false positive, and false negative predictions. (a) RetinaNet, FCOS, and Rotated RPN statically assign labels between fixed priors and fixed *gts*. (b) Our proposed DCFL dynamically updates priors and *gts*, and dynamically assigns labels.

tors are quite remarkable. Especially, the extreme geometry characteristics of oriented tiny objects hamper the accurate label assignment.

Label assignment is a fundamental and crucial process in object detection [68], in which priors (box for anchor-based [30] and point for anchor-free detectors [50]) need to be assigned with appropriate labels to supervise the network training. In fact, there have been some works that lay a foundation for the effective label assignment of oriented objects, as shown in Fig. 1. Early works additionally preset anchors of different angles (*e.g.* Rotated RPN [36]) or refine high-quality anchors (*e.g.* S²A-Net [17]) based on the generic object detector, then a static rule (*e.g.* MaxIoU strategy [44]) is used to separate positive and negative (*pos/neg*) training samples. The derived prior boxes can thus cover more ground truth (*gt*) boxes and a considerable accuracy improvement can be expected. However, the static assignment cannot adaptively divide *pos/neg* samples according to the *gt's* shape and filter out low-quality samples, usually
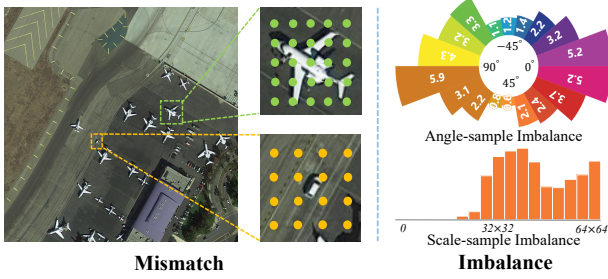
Figure 2. The mismatch and imbalance issues. Each point in the left image denotes a prior location. The number in the pie-shaped bar chart denotes the mean number of positive samples assigned to each instance in a specific angle range.

leading to sub-optimal performance.

Recently, the exploration of adaptive label assignment [68] brings new insight to the community. For oriented object detection, DAL [38] defines a prediction-aware matching degree and utilizes it to reweight anchors, achieving dynamic sample learning. Besides, several studies [21,23,26] incorporate the shape information into detectors and propose shape-aware sampling and measurement.

Despite the progress, the arbitrary orientation and extreme size of oriented tiny objects still pose a dilemma to the detector. As shown in Fig. 2, the **mismatch** and **imbalance** issues are particularly pronounced. For one thing, there is a mutual mismatch issue between the *position prior*, *feature*, and *instance*. Although some adaptive label assignment schemes may explore a better *pos/neg* division of the prior boxes or points, the sampled feature location behind the prior is still fixed and the derived prior is still static and uniformly located, most priors deviate from the tiny object's main body. The prior and feature themselves cannot well-match the extreme shapes of oriented tiny objects, no matter how we divide *pos/neg* samples. For another, the existing detectors tend to introduce bias and imbalance for oriented and tiny objects. More precisely, for anchor-based detectors, *gt* with shapes different from anchor boxes will yield low IoU [38,59], leading to the lack of positive samples. In Fig. 2, we calculate the mean number of positive samples assigned to different *gts* with the RetinaNet and observe that there is an extreme lack of positive samples for *gts* with angles and scales far from predefined anchors. For anchor-free detectors, the static prior and its fixed stride limit the upper number of high-quality positive samples. Tiny objects only cover a limited number of feature points, and most of these points are away from the object's main body.

This motivates us to design a more dynamic and balanced learning pipeline for oriented tiny object detection. As shown in Fig. 1, we alleviate the mismatch issue by reformulating the prior, label assignment, and *gt* representation all in a dynamic manner, which can be updated by the Deep Neural Network (DNN). Simultaneously, we dynamically and progressively assign labels in a coarse-to-fine manner to seek balanced supervision for various instances.

Specifically, we introduce a dynamic Prior Capturing Block (PCB) to learn the prior, which adaptively adjusts the prior location while retaining the physical meaning of prior [54]. The PCB is inspired by the paradigm of learnable proposals in the DETR [4] and Sparse R-CNN [48] which naturally avoids the mismatch issue between the predefined prior and feature. Compared to this paradigm, we introduce its flexibility for prior updates while keeping the fast-convergence ability of dense detectors [32, 54]. Based on the dynamic prior, we then select Cross-FPN-layer Coarse Positive Sample (CPS) candidates for further label assignment, and the CPS is realized by the Generalized Jensen-Shannon Divergence [39] (GJSD) between the *gt* and the dynamic prior. The GJSD is able to enlarge the CPS to the object's nearby spatial locations and adjacent FPN layers, ensuring more candidates for extreme-shaped objects. After obtaining the CPS, we re-rank these candidates with predictions (posterior) and represent the *gt* with a finer Dynamic Gaussian Mixture Model (DGMM), filtering out low-quality samples. All designs are incorporated into an end-to-end one-stage detector without additional branches.

In short, our contributions are listed as follows: (1) We identify that there exist severe mismatch and imbalance issues in the current learning pipeline for oriented tiny object detection. (2) We design a Dynamic Coarse-to-Fine Learning (DCFL) scheme for oriented tiny object detection, which is the first to model the prior, label assignment, and *gt* representation all in a dynamic manner. In the DCFL, we propose to use the GJSD to construct Coarse Positive Samples (CPS) and represent objects with a finer Dynamic Gaussian Mixture Model (DGMM), obtaining coarse-to-fine label assignment. (3) Extensive experiments on six datasets show promising results.

2. Related Work

2.1. Oriented Object Detection

Prior for Oriented Objects. Anchor, as a classic design in generic object detectors (*e.g.* Faster R-CNN [44], RetinaNet [30]), has facilitated object detection for a long time. Similarly, oriented object detection also benefits from the anchor design. Initially, rotated RPN [36] extends the RPN to the field of oriented object detection by tiling 54 anchors each location with preset angles and scales. Indeed, enumerating potential *gt* shapes can notably improve the recall, apart from the sacks of additional computational cost. RoI Transformer [10] utilizes horizontal anchors and transforms the RPN-generated horizontal proposals to oriented proposals, reducing the number of rotated anchors. To save computation, the Oriented R-CNN [56] introduces an ori-

ented RPN that directly predicts oriented proposals based on horizontal anchors. Recently, one-stage oriented object detectors gradually emerged, including anchor-based detectors [17, 60] with box prior and anchor-free detectors [26, 28] with point prior. Most of them retain the fixed prior design, except for the S^2A-Net [17] which proposes to generate high-quality anchors.

Label Assignment. ATSS [68] reveals that label assignment plays a pivotal role in the detectors' performance [14, 24, 37]. In the field of oriented object detection, DAL [38] observes inconsistency between the input prior IoU and the output predicted IoU, then defines a matching degree as the soft label that dynamically reweights anchors. Recently, SASM [21] introduces a shape-adaptive sample selection and measurement strategy to improve detection performance. Similarly, GGHL [23] proposes to fit the main body of the instance by a single 2-D Gaussian heatmap, then it divides and reweights samples in a dynamic manner. In addition, Oriented Reppoints [26] improves the RepPoints [65] by assessing the quality of points for more effective label assignment.

2.2. Tiny Object Detection

Multi-scale Learning. Basically, one can use a multi-resolution image pyramid to obtain multi-scale learning. However, the vanilla image pyramid will bring much computation cost. Thus, some works [29, 33, 34, 42, 49, 69] reduce computation with the efficient Feature Pyramid Network (FPN). Unlike the FPN, TridentNet [27] introduces multi-branch detection heads of various receptive fields for multi-scale prediction. Moreover, one can normalize the scale of objects for scale-invariant object detection, for example, SNIP [46] and SNIPER [47] resize images and train objects within a certain scale range.

Label Assignment. Tiny objects usually have low IoU with anchors or cover a limited number of feature points, thus suffering from the lack of positive samples. ATSS [68] slightly reconciles the number of positive samples for objects of different scales. NWD [57] designs a new metric to replace IoU, which can sample more positive samples for tiny objects. Recently, the RFLA [58] utilizes outliers to detect tiny objects for scale-balanced learning.

Context Information. Tiny object lacks discriminative features, but objects are closely related to the surrounding context. Therefore, we can leverage the context information to enhance small object detection. Muti-Region CNN (MRCNN) [15] and Inside-Outside Network (ION) [3] are two representative works that exploit local and global context information. Recently, the Relation Network [22] and transformer-based detectors [4, 54, 72] reason about the association between instances via the attention mechanism.

Feature Enhancement. The feature representation of small objects can be enhanced by super-resolution or GAN.

PGAN [25] first applies GAN to small object detection. Besides, Bai *et al.* [1] introduce the MT-GAN which trains an image-level super-resolution model to improve the RoI features of small objects. In addition, there are some other methods based on super-resolution including [2, 8, 40, 43].

By contrast, our method simultaneously handles the prior mismatch and unbalanced learning via dynamically modeling the prior, label assignment, and *gt* representation. Meanwhile, unlike the two-stage RoI-Transformer [10] or one-stage S^2A-Net [17], we embed the dynamic prior inside the end-to-end one-stage detector without introducing any auxiliary branch.

3. Method

Overview. Given a set of dense prior $P \in \mathbb{R}^{W \times H \times C}$ ($W \times H$ is the feature map size, C is the shape information number, each feature point has one prior for simplicity), object detectors remap the set P into final detection results D through the Deep Neural Network (DNN), which can be simplified as:

$$D = \text{DNN}_h(P), \tag{1}$$

where DNN_h denotes the detection head. Detection results D contain two parts: classification scores $D_{cls} \in \mathbb{R}^{W \times H \times A}$ (A is the class number) and box locations $D_{reg} \in \mathbb{R}^{W \times H \times B}$ (B is the box parameter number).

To train the DNN_h, we need to find a proper matching between the prior set P and the *gt* set GT, and assign *pos/neg* labels to P to supervise the network learning. For static assigners (*e.g.* RetinaNet [30]), the set of *pos* labels G can be obtained via hand-crafted matching function $\mathcal{M}_s$:

$$G = \mathcal{M}_s(P, GT). \tag{2}$$

For dynamic assigners [14, 24, 38], they tend to simultaneously leverage the prior information P and posterior information (predictions) D, and then apply a prediction-aware mapping $\mathcal{M}_d$ to get the set G:

$$G = \mathcal{M}_d(P, D, GT). \tag{3}$$

After the *pos/neg* label separation, the loss function can be summarized into two parts:

$$\mathcal{L} = \sum_{i=1}^{N_{pos}} \mathcal{L}_{pos}(D_i, G_i) + \sum_{j=1}^{N_{neg}} \mathcal{L}_{neg}(D_j, y_j), \tag{4}$$

where N_{pos}, N_{neg} are the number of positive and negative samples respectively, y_j denotes the negative label.

While in this work, we model the prior, label assignment, and *gt* representation all in a dynamic manner to alleviate the mismatch issue. To begin with, the dynamic prior is reformulated to (˜denotes the dynamic item):

$$\tilde{D} = \text{DNN}_h(\underbrace{\text{DNN}_p(P)}_{\text{Dynamic Prior } \tilde{P}}), \tag{5}$$

DNN_p is a learnable block incorporated within the detection head to update the prior. Then, the matching function is reformulated to a coarse-to-fine paradigm:

$$\tilde{G} = \mathcal{M}_d(\mathcal{M}_s(\tilde{P}, GT), \tilde{GT}), \qquad (6)$$

the $\tilde{GT}$ is a finer representation of an object with the Dynamic Gaussian Mixture Model (DGMM). In a nutshell, our final loss is modeled as:

$$\mathcal{L} = \sum_{i=1}^{\tilde{N}_{pos}} \mathcal{L}_{pos}(\tilde{D}_i, \tilde{G}_i) + \sum_{j=1}^{\tilde{N}_{neg}} \mathcal{L}_{neg}(\tilde{D}_j, y_j). \qquad (7)$$

3.1. Dynamic Prior

Inspired by the purely learnable paradigm of proposal updation in the DETR [4] and Sparse R-CNN [48], we propose to introduce more flexibility into the prior to mitigate the mismatch issue. Moreover, we retain the physical meaning of prior where each individual prior stands for a feature point, inheriting the fast convergence ability of dense detectors. The structure of the proposed Prior Capturing Block (PCB) is shown in Fig. 3, in which a dilated convolution is deployed to take the surrounding information into account, and then the Deformable Convolution Network (DCN) [9] is leveraged to capture the dynamic prior. Besides, we utilize the learned offsets from the regression branch to guide the feature extraction of the classification branch, leading to better alignment between the two tasks.

The dynamic prior capturing process is as follows. First of all, we initialize each prior location $\mathbf{p}(x, y)$ by each feature point's spatial location $\mathbf{s}$ (which is remapped to the image). In each iteration, we forward the network to capture the offset sets of each prior location $\Delta\mathbf{o}$. Hence, the prior spatial location can be updated by:

$$\tilde{\mathbf{s}} = \mathbf{s} + st \sum_{i=1}^{n} \Delta\mathbf{o}_i / 2n, \qquad (8)$$

where st is the feature map's stride, n is the number of offsets. Finally, we utilize the 2-D Gaussian distribution $\mathcal{N}_p(\boldsymbol{\mu}_p, \boldsymbol{\Sigma}_p)$ which is demonstrated conducive to small objects [58,61] and oriented objects [61,63] to fit the prior spatial location. Concretely, the dynamic $\tilde{\mathbf{s}}$ serves as the Gaussian's mean vector $\boldsymbol{\mu}_p$. We preset one prior which is square-shaped (w, h, θ) as that in RetinaNet [30] on each feature point, then compute the co-variance matrix $\boldsymbol{\Sigma}_p$ by [64]:

$$\boldsymbol{\Sigma}_p = \begin{bmatrix} \cos\theta & -\sin\theta \\ \sin\theta & \cos\theta \end{bmatrix} \begin{bmatrix} \frac{w^2}{4} & 0 \\ 0 & \frac{h^2}{4} \end{bmatrix} \begin{bmatrix} \cos\theta & \sin\theta \\ -\sin\theta & \cos\theta \end{bmatrix}. \quad (9)$$

3.2. Coarse Prior Matching

Given a set of prior, one basic assignment rule is to specify a range of candidate true prediction samples for a specific gt. Some adaptive strategies restrict the candidates of a given gt inside a single FPN layer [14,23,68], while some

works release all layers as candidates [67, 71]. However, for oriented tiny objects, the former strict heuristic rule may lead to a sub-optimal layer selection and the latter loose one will induce the slow convergence issue [32].

Hence, we propose Cross-FPN-layer Coarse Positive Sample (CPS) candidates, which narrows down the sample range compared to the all-FPN-layer manner while discarding the single-layer heuristic. In the CPS, we slightly expand the range of candidates to the gt's nearby spatial location and adjacent FPN layers, which warrants relatively diverse and sufficient candidates compared to the single-layer heuristic and alleviates the quantity imbalance issue.

Specifically, the similarity measurement in constructing the CPS is realized with the Jensen-Shannon Divergence (JSD) [13], which inherits the scale invariance property of the Kullback–Leibler Divergence (KLD) [63] and can measure the gt's similarity with nearby non-overlapping priors [58, 63]. Moreover, it conquers KLD's drawback of asymmetry. However, the closed-form solution of the JSD between Gaussian distributions is unavailable [39], thus, we utilize the Generalized Jensen-Shannon Divergence (GJSD) [39] which yields a closed-form solution, as the substitute.

For example, the GJSD between two Gaussian distributions $\mathcal{N}_p(\boldsymbol{\mu}_p, \boldsymbol{\Sigma}_p)$ and $\mathcal{N}_g(\boldsymbol{\mu}_g, \boldsymbol{\Sigma}_g)$ is defined by:

$$\text{GJSD}(\mathcal{N}_p, \mathcal{N}_g) = (1 - \alpha)\text{KL}(\mathcal{N}_\alpha, \mathcal{N}_p) + \alpha\text{KL}(\mathcal{N}_\alpha, \mathcal{N}_g), \qquad (10)$$

where KL denotes the KLD, and $\mathcal{N}_\alpha(\boldsymbol{\mu}_\alpha, \boldsymbol{\Sigma}_\alpha)$ is given by:

$$\boldsymbol{\Sigma}_\alpha = (\boldsymbol{\Sigma}_p \boldsymbol{\Sigma}_g)_\alpha^{\boldsymbol{\Sigma}} = \left((1 - \alpha)\boldsymbol{\Sigma}_p^{-1} + \alpha\boldsymbol{\Sigma}_g^{-1}\right)^{-1}, \quad (11)$$

and

$$\begin{aligned} \boldsymbol{\mu}_\alpha &= (\boldsymbol{\mu}_p \boldsymbol{\mu}_g)_\alpha^{\boldsymbol{\mu}} \\ &= \boldsymbol{\Sigma}_\alpha \left((1 - \alpha)\boldsymbol{\Sigma}_p^{-1}\boldsymbol{\mu}_p + \alpha\boldsymbol{\Sigma}_g^{-1}\boldsymbol{\mu}_g\right). \end{aligned} \qquad (12)$$

Note that α is a parameter that controls the weight of two distributions [39] in similarity measurement. In our work, the $\mathcal{N}_p$ and $\mathcal{N}_g$ contribute equally, thus α is set to 0.5.

Ultimately, for each gt, we select K priors which hold the top K GJSD score with this gt as the Coarse Positive Samples (CPS) and regard the remaining priors as negative samples, this coarse matching serves as the $\mathcal{M}_s$ in Eq. 6. The ranking manner works together with the GJSD measurement to construct the Cross-FPN-layer CPS, eliminating the imbalance issue raised by the MaxIoU matching for outlier angles and scales, which will be analyzed in Sec. 5.

3.3. Finer Dynamic Posterior Matching

Based on Coarse Positive Sample (CPS) candidates, we design a dynamic posterior (prediction) matching rule $\mathcal{M}_d$ to filter out low-quality samples. The $\mathcal{M}_d$ consists of two key components, namely a posterior re-ranking strategy and a Dynamic Gaussian Mixture Model (DGMM) constraint.

Figure 3. The process of feature extraction and dynamic coarse-to-fine learning. PCB denotes the prior capturing block.

We re-rank the sample candidates in the CPS according to their predicted scores. In other words, we further refine the positive samples by their Possibility of becoming True predictions (PT) [14], which is a linear combination of the predicted classification score and the location score with the gt. We define the PT of the ith sample D_i as:

$$PT_i = \frac{1}{2}Cls(D_i) + \frac{1}{2}IoU(D_i, gt_i), \qquad (13)$$

where Cls is the predicted classification confidence and IoU is the rotated IoU between the predicted location and its corresponding gt location. We select candidates with Q highest PT as Medium Positive Sample (MPS) candidates.

Following this, we filter out those samples too far away from the gts with a finer instance representation, getting the Finer Positive Samples (FPS). Different from previous works which utilize the center probability map [53] or the single-Gaussian [23,64] for instance representation, we represent the instance by a finer DGMM. It consists of two components: one is centered on the geometry center and the other is centered on the semantic center of the object. Concretely, for a specific instance gt_i, the geometry center (cx_i, cy_i) serves as the mean vector $\boldsymbol{\mu}_{i,1}$ of the first Gaussian, and the semantic center (sx_i, sy_i), which is deduced by averaging the location of the samples in the MPS, serves as the $\boldsymbol{\mu}_{i,2}$. That is to say, we parameterize the instance as:

$$DGMM_i(s|x,y) = \sum_{m=1}^{2} w_{i,m}\sqrt{2\pi|\boldsymbol{\Sigma}_{i,m}|}\mathcal{N}_{i,m}(\boldsymbol{\mu}_{i,m}, \boldsymbol{\Sigma}_{i,m}), \qquad (14)$$

where $w_{i,m}$ is the weight of each Gaussian with a summation of 1, $\boldsymbol{\Sigma}_{i,m}$ equals to the gt's $\boldsymbol{\Sigma}_g$. Each sample in MPS has a DGMM score $DGMM(s|MPS)$, we set negative masks to samples which have $DGMM(s|MPS) < e^{-g}$ with any gt, the g is adjustable.

4. Experiments

4.1. Datasets

Experiments are done on six datasets, *i.e.*, DOTA-v1.0 [55]/v1.5/v2.0 [11], DIOR-R [7], VisDrone [12], and

MS COCO [31]. In ablation studies and analyses, we choose the large-scale DOTA-v2.0 `train set` for training and `val set` for evaluation, which contains a large number of tiny objects. To compare with other methods, we use `trainval sets` of DOTA-v1.0, DOTA-v1.5, DOTA-v2.0, and DIOR-R for training and their `test sets` for testing, we choose the VisDrone2019, MS COCO `train set`, `val set` for training and testing.

4.2. Implementation Details

We conduct all the experiments on the computer with a single NVIDIA RTX 3090 GPU, and the batch size is set to 4. Models are built based on MMDetection [6] and MMRotate [70] with PyTorch [41]. The ImageNet [45] pre-trained models are used as the backbone. The Stochastic Gradient Descent (SGD) optimizer is used for training with a learning rate of 0.005, a momentum of 0.9, and a weight decay of 0.0001. The ResNet-50 [20] with FPN [29] is the default backbone if not specified. We use Focal loss [30] for classification and IoU loss [66] for regression. We only use random flipping as data augmentation for all experiments.

For experiments on the DOTA-v1.0 and DOTA-v2.0, we follow the official settings of the DOTA-v2.0 benchmark [11], *i.e.*, we crop images into patches of 1024×1024 with overlaps of 200 and train the model for 12 epochs. For DOTA-v2.0, we reproduce one-stage state-of-the-art methods [17,21,26,38,50,60,63,68] with the same settings.

For experiments on other datasets, we set the input size to 1024×1024 (overlap 200), 800×800, 1333×800, and 1333×800 for DOTA-v1.5, DIOR-R, VisDrone, and COCO respectively. We train the models for 40, 40, 12, and 12 epochs on the DOTA-v1.5, DIOR-R, COCO, and VisDrone as previous works do [16,26]. The above settings are fixed unless otherwise specified.

4.3. Main Results

Results on DOTA series. As shown in Tab. 1, our proposed method achieves the state-of-the-art performance of 57.66% mAP on the DOTA-v2.0 OBB benchmark un-

Table 1

Method	Backbone	Plane	BD	Bridge	GTF	SV	LV	Ship	TC	BC	ST	SBF	RA	Harbor	SP	HC	CC	Air	Heli	mAP
multi-stage:																				
FR OBB [44]	R50	71.61	47.20	39.28	58.70	35.55	48.88	51.51	78.97	58.36	58.55	36.11	51.73	43.57	55.33	57.07	3.51	52.94	2.79	47.31
FR OBB + Dp	R50	71.55	49.74	40.34	60.40	40.74	50.67	56.58	79.03	58.22	58.24	34.73	51.95	44.33	55.10	53.14	7.21	59.53	6.38	48.77
MR [19]	R50	76.20	49.91	41.61	60.00	41.08	50.77	56.24	78.01	55.85	57.48	36.62	51.67	47.39	55.79	59.06	3.64	60.26	8.95	49.47
HTC* [5]	R50	77.69	47.25	41.15	60.71	41.77	52.79	58.87	78.74	55.22	58.49	38.57	52.48	49.58	56.18	54.09	4.20	66.38	11.92	50.34
RT [10]	R50	71.81	48.39	45.88	64.02	42.09	54.39	59.92	82.70	63.29	58.71	41.04	52.82	53.32	56.18	57.94	25.71	63.72	8.70	52.81
Oriented R-CNN [56]	R50	77.95	50.29	46.73	65.24	42.61	54.56	60.02	79.08	61.69	59.42	42.26	56.89	51.11	56.16	59.33	25.81	60.67	9.17	53.28
one-stage:																				
DAL [38]	R50	71.23	38.36	38.60	45.24	35.42	43.75	56.04	70.84	50.87	56.63	20.28	46.53	33.49	47.29	12.15	0.81	25.77	0.00	38.52
SASM [21]	R50	70.30	40.62	37.01	59.03	40.21	45.46	44.60	78.58	49.34	60.73	29.89	46.57	42.95	48.31	28.13	1.82	76.37	0.74	44.53
RetinaNet-O [30]	R50	70.63	47.26	39.12	55.02	38.10	40.52	47.16	77.74	56.86	52.12	37.22	51.75	44.15	53.19	51.06	6.58	64.28	7.45	46.68
R³Det w/ KLD [63]	R50	75.44	50.95	41.16	61.61	41.11	45.76	49.65	78.52	54.97	60.79	42.07	53.20	43.08	49.55	34.09	36.26	68.65	0.06	47.26
FCOS-O [51]	R50	74.84	47.53	40.83	57.41	43.89	47.72	55.66	78.61	57.86	63.00	38.02	52.38	41.91	53.24	40.22	7.15	65.51	7.42	48.51
Oriented Rep [26]	R50	73.02	46.68	42.37	63.05	47.06	50.28	58.64	78.84	57.12	66.77	35.21	50.76	48.77	51.62	34.23	6.17	64.66	5.87	48.95
ATSS-O [68]	R50	77.46	49.55	42.12	62.61	45.15	48.40	51.70	78.43	59.33	62.65	39.18	52.43	42.92	53.98	42.70	5.91	67.09	10.68	49.57
S²A-Net [17]	R50	77.84	51.31	43.72	62.59	47.51	50.58	57.86	80.73	59.11	65.32	36.43	52.60	45.36	52.46	40.12	0.00	62.81	11.11	49.86
one-stage:																				
DCFL	R50	75.71	49.40	44.69	63.23	46.48	51.55	55.50	79.30	59.96	65.39	41.86	54.42	47.03	55.72	50.49	11.75	69.01	7.75	51.57
S²A-Net w/ DCFL	R50	74.79	53.25	45.81	65.46	46.49	53.23	58.10	81.51	60.13	66.42	43.24	55.09	50.52	55.58	54.53	5.23	68.73	13.06	52.84
DCFL†	R50	78.30	53.03	44.24	60.17	48.56	55.42	58.66	78.29	60.89	65.93	43.54	55.82	53.33	60.00	54.76	30.90	74.01	15.60	55.08
DCFL†	ReR101	79.49	55.97	50.15	61.59	49.00	55.33	59.31	81.18	66.52	60.06	52.87	56.71	57.83	58.13	60.35	35.66	78.65	13.03	57.66

Table 1. Main results on the DOTA-v2.0 OBB Task. We follow the official class abbreviations as the DOTA-v2.0 benchmark [11]. † denotes training for 40 epochs. Note that this paper [63] reports 50.90% mAP for R³Det w/ KLD under 20 epochs, the ReR101 backbone is proposed by the ReDet [18]. The results in red and blue denote the best and second-best performance of each column.

Method	CFA [16]	RetinaNet-O [30]	R³Det [60]	Oriented Rep [26]	ATSS-O [68]
mAP	69.63	69.79	70.18	71.94	72.29
Method	KLD [63]	S²A-Net [17]	GGHL [23](3x)	DCFL	DCFL(3x)
mAP	72.76	73.91	73.98	74.26	**75.35**

Table 2. Comparison with one-stage detectors on the DOTA-v1.0 OBB Task. All results are based on the MMRotate [70] with 12 epochs except for GGHL [23]. 3x means training for 36 epochs.

Method	Backbone	SV	Ship	ST	mAP
RetinaNet-O [30]	R50	44.53	73.31	59.96	59.16
FR OBB [19]	R50	51.28	79.37	67.50	62.00
CMR [19]	R50	51.64	79.99	67.58	63.41
RT [10]	R50	52.05	80.72	68.26	65.03
ReDet [18]	ReR50	52.38	80.92	68.64	66.86
DCFL	R50	56.72 (+12.19)	80.87 (+7.56)	75.65 (+15.69)	67.37 (+8.21)
DCFL	ReR101	57.31 (+12.78)	86.60 (+13.29)	76.55 (+16.59)	70.24 (+11.08)

Table 3. Main results on the DOTA-v1.5 OBB Task.

Method	RetinaNet-O [30]	FR-OBB [44]	RT [10]	AOPG [7]
mAP	57.55	59.54	63.87	64.41
Method	GGHL [23]	Oriented Rep [26]	DCFL	DCFL (ReR101)
mAP	66.48	66.71	66.80	**71.03**

Table 4. Performance comparisons on the DIOR-R dataset.

Method	Backbone	VE	BR	WM
RetinaNet-O [30]	R50	38.0	24.0	60.2
Oriented Rep [26]	R50	50.4	38.8	64.7
DCFL	R50	50.9 (+12.9)	42.1 (+18.1)	70.9 (+10.7)

Table 5. Detection results of typical tiny objects on the DIOR-R dataset. VE, BR, and WM denote vehicle, bridge, and wind-mill.

Dataset	VisDrone		MS COCO		DOTA-v2.0 HBB	
Method	RetinaNet [30]	DCFL	RetinaNet	DCFL	FCOS [58]	DCFL
$AP_{0.5}$	29.2	32.1	55.4	57.3	55.4	57.4

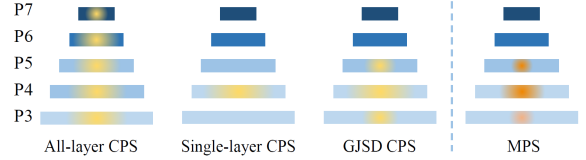Table 6. Results of one-stage object detectors on HBB datasets.

Figure 4. Different ways of constructing the CPS. Yellow and orange denote the possible regions of CPS and MPS respectively.

Results also indicate that our DCFL is very effective for detecting tiny oriented objects on the tested datasets, such as small vehicles, ships, and storage tanks, where a boost of about 10 points can be expected compared to the baseline.

Results on DIOR-R. DIOR-R contains some tiny oriented objects, such as the vehicle, bridge, and windmill. The mAP and class-wise AP of tiny objects are in Tab. 4 and Tab. 5, we also achieve the state-of-the-art performance of 71.03% mAP and notable improvements on tiny objects.

Results on HBB Datasets. Moreover, we discard the angle to verify the versatility of the DCFL on the generic small object detection datasets VisDrone [12], MS COCO [31], and DOTA-v2.0 HBB [11]. In Tab. 6, our method gets a notable $AP_{0.5}$ boost compared to the baseline.

4.4. Ablation Study

Effects of Individual Strategy. We check the effectiveness of each proposed strategy in the proposed method. In

der single-scale training and testing. Besides, our model achieves 51.57% mAP without bells and whistles, surpassing all one-stage object detectors tested. The results on the DOTA-v1.0 [55] and DOTA-v1.5 are listed in Tab. 2, Tab. 3.

Method	CPS	MPS	DGMM	mAP
baseline [30]				51.70
DCFL	✓	✓		53.41
	✓		✓	57.20
	✓	✓	✓	**59.15**

(a) **Individual effectiveness.** CPS, MPS, and DGMM denote Coarse, Medium Sample Candidates and Dynamic Gaussian Mixture Model.

Strategy	Measurement	mAP
All-FPN-layer	Gaussian	50.12
Single-FPN-layer	Gaussian	56.72
Cross-FPN-layer	KLD [63]	57.82
Cross-FPN-layer	GWD [61]	58.55
Cross-FPN-layer	GJSD	**59.15**

(b) **Comparisons of different CPS.** The FPN layer number varies for different strategies of getting the CPS.

DCN	Dilated Conv	DP	mAP
			58.07
✓			58.41
✓	✓		58.65
Separate	✓	✓	58.71
Guiding	✓	✓	**59.15**

(c) **Effects of detailed designs in the PCB.** DP denotes the dynamic prior. Guiding denotes *reg* guides *cls*.

K		24				20		
Q	20	16	12	8	16	12	10	8
mAP	58.31	58.11	58.95	59.06	58.66	58.71	58.92	58.28
K		16				12		
Q	12	10	8	6	10	8	6	4
mAP	**59.15**	58.57	58.97	57.84	58.79	58.25	57.01	57.37

(d) **Effects of parameters K and Q.**

g	1.2	1.0
mAP	57.91	58.20
g	0.8	0.4
mAP	**59.15**	58.95

(e) **Effects of parameter g.**

Table 7. **Ablations**. We train on DOTA-v2.0 `train set`, test on `val set`, and report mAP under IoU threshold 0.5.

all ablation experiments, we employ one prior for each feature point for fair comparisons. As seen in Tab. 7a, the baseline detector RetinaNet-OBB yields a result of 51.70% mAP. When we gradually apply the posterior re-ranked MPS and DGMM into the detector based on the CPS, the mAP improves progressively, verifying each design's effectiveness. Note that the CPS cannot be independently used since the samples in it are too coarse to serve as the final positive samples. Nevertheless, we compare some different ways of constructing the CPS to verify its superiority.

Comparisons of Different CPS. The design of the CPS matters in the training pipeline. We show several paradigms of designing the CPS as shown in Fig. 7b, including limiting the CPS for a specific *gt* within a single layer, releasing all FPN layers as the CPS, like Objectbox [67]. We compare their performance in Tab. 7b. For fair comparisons, the number of samples in CPS is fixed at 16, and all other components are kept the same. For the Single-FPN-layer way, we group *gt* onto different layers according to the scale division strategy in FCOS, then assign labels within each layer. For the All-FPN-layer way, we do not group *gt* onto different layers, instead, we discard the prior scale information and directly measure the distance between Gaussian *gt* and prior points. The results are shown in Tab. 7b, we can observe that neither of the above two ways will yield the best performance. By contrast, the distribution distances (KLD, GWD, GJSD) are able to construct the Cross-FPN-layer CPS, where the candidates are extended to adjacent layers besides the main layer. We can also see the GJSD gets the best performance of 59.15% mAP, mainly resulting from its property of scale-invariance [39, 63], symmetry [39], and ability to measure non-overlapping boxes [39] compared to other counterparts.

Fixed Prior and Dynamic Prior. We conduct a finer group of ablation studies to verify the necessity of introducing the dynamic prior. As shown in Tab. 7c, if we disable the dynamic prior by fixing the location of samples, a slight performance drop will be introduced. Hence, the prior should be adjusted accordingly when leveraging the dynamic sampling strategy to better capture the shape of objects.

Detailed Design in PCB. For the PCB, it is made up of a dilated convolution and a guiding DCN, we slightly enlarge the receptive field with a dilation rate of 3. After that, we take advantage of the DCN to generate dynamic priors in a guiding manner. As shown in Tab. 7c, we can observe that the DCN can bring an improvement of 0.34 mAP points and the dilated convolution can slightly enhance the mAP. We find that the application of the DCN [9] to the single regression branch will slightly deteriorate the accuracy (noted by *Separate* in Tab. 7c), which may cause mismatch issues between the two branches. Thus we utilize the offsets from the regression head to guide the offsets classification head for better alignment (noted by *Guiding*).

Effects of Parameters. The introduced three parameters are robust in a certain range. From Tab. 7d, we can see that a combination of $K = 16$ and $Q = 12$ gets the best performance. In Tab. 7e, we verify the threshold e^{-g} in the DGMM, we empirically set $w_{i,1}$ to 0.7, then a threshold of $g = 0.8$ yields the highest mAP. Although making the CPS/MPS/FPS coarser and stricter will weaken the performance, the mAP only waves marginally. In other words, the coarse-to-fine assignment manner somewhat warrants the parameter selection's robustness since multiple parameters can attenuate the effects of an under-tuned one.

5. Analysis

For a clearer dissection of why the proposed scheme works, we perform more meticulous analyses as follows.

Reconciliation of imbalance problems. To delve into the imbalance issue, we calculate the mean predicted IoU and the mean positive sample number of *gt* holding differ-
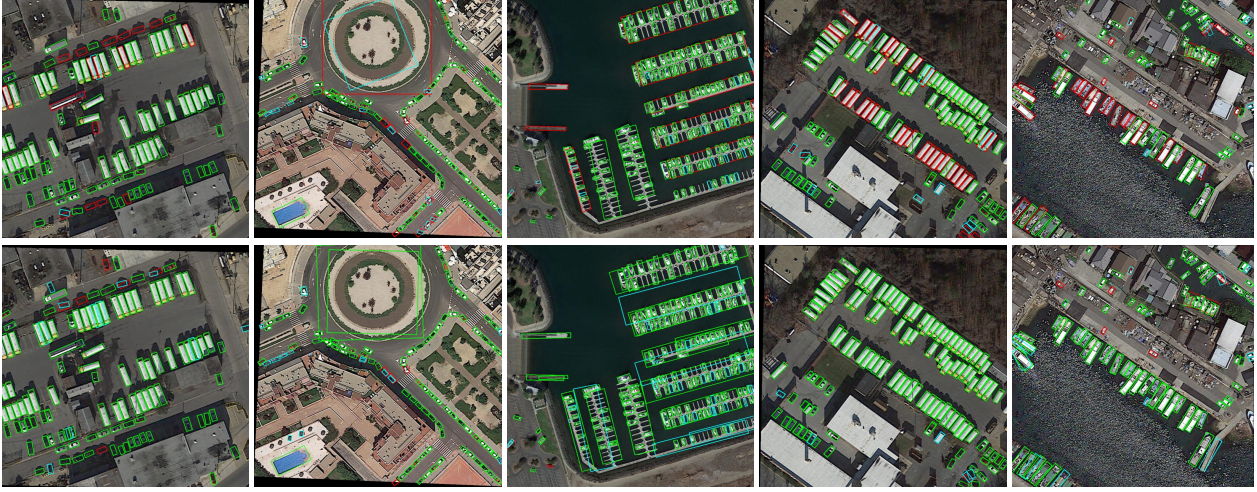
Figure 5. Visualization analysis of the predicted results. The first row is the result of the RetinaNet-OBB while the second row is the result of the DCFL. TP, FN, and FP predictions are marked in green, red, and blue respectively.
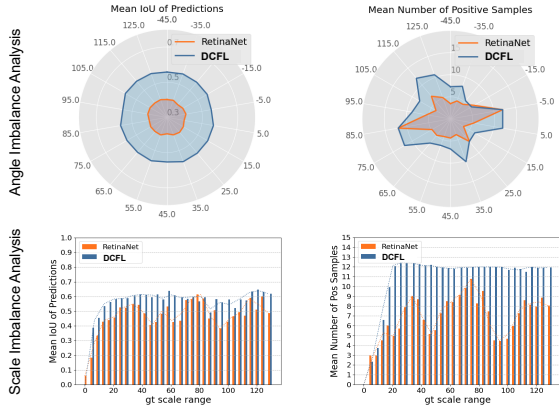

Figure 6. Statistical analysis of imbalance issues. The first and second columns show quality and quantity imbalance respectively.

Figure 7. Visualization of sampled dynamic priors.

Method	R^{3}Det [60]	S^{2}A-Net [17]	GA-RetinaNet [52]	RetinaNet [30]	DCFL
Params, GFLOPs	42.0M, 337.3	38.6M, 197.9	37.4M, 206.9	36.5M, 217.3	**36.1M, 157.8**

Table 8. Comparison of *params*, GFLOPs with 1024×1024 input.

positive samples in Fig. 5 and Fig. 7. We can see that the DCFL remarkably eliminates the False Negative and False Positive predictions, especially for the extreme-shaped oriented tiny objects. Fig. 7 shows that the proposed strategy is able to dynamically generate and sample priors that better fit the instance's main body, verifying the claims of dynamic modeling and mismatch alleviation in this work.

Speed. We test the inference speed on DOTA-v2.0 `val set` with a single RTX3090 GPU, the FPS of the R^{3}Det, S^{2}A-Net, RetinaNet, and DCFL is 16.2, 18.9, 20.8, and 20.9. It indicates that our method is of high efficiency. Moreover, we provide the parameters and GLOPs in Tab. 8, where we can see that the DCFL is lighter.

6. Conclusion

In this paper, we propose a novel DCFL scheme for detecting oriented tiny objects. We identify that the mismatched feature prior and unbalanced positive samples are two obstacles hampering the label assignment for oriented tiny objects. To address these, we propose a dynamic prior to alleviate the mismatch issue and a coarse-to-fine assigner to mitigate the imbalance issue, where the prior, label assignment, and *gt* representation are all reformulated in a dynamic manner. Extensive experiments and analyses show the convincing improvements brought by the DCFL.

Acknowledgement

ent angles and different scales (absolute size). Results are shown in Fig. 6, which are from the models' last training epoch. Here we summarize two kinds of imbalance issues (quantity and quality imbalance) for RetinaNet: (1) The positive sample number assigned to each instance changes periodically *w.r.t.* its angle and scale, whereas objects with shapes (scale, angle) different from predefined priors will hold much fewer positive samples. (2) The predicted IoU changes periodically *w.r.t. gt*'s scale while remaining invariant *w.r.t. gt*'s angle. By contrast, DCFL remarkably reconciles the imbalance: (1) more positive samples are compensated to previously outlier angles and scales. (2) the samples' quality (predicted IoU) can also be improved and balanced across all angles and scales. The above results are the desired behavior of dynamic coarse-to-fine learning.

Visualization. We visualize the predicted results and

References

[1] Yancheng Bai, Yongqiang Zhang, Mingli Ding, and Bernard Ghanem. Sod-mtgan: Small object detection via multi-task generative adversarial network. In *European Conference on Computer Vision*, pages 206–221. Springer, 2018. 3

[2] Syed Muhammad Arsalan Bashir and Yi Wang. Small object detection in remote sensing images with residual feature aggregation-based super-resolution and object detector network. *Remote Sensing*, 13(9):1854, 2021. 3

[3] Sean Bell, C Lawrence Zitnick, Kavita Bala, and Ross B Girshick. Inside-Outside Net: Detecting objects in context with skip pooling and recurrent neural networks. In *IEEE Conference on Computer Vision and Pattern Recognition*, pages 2874–2883, 2016. 3

[4] Nicolas Carion, Francisco Massa, Gabriel Synnaeve, Nicolas Usunier, Alexander Kirillov, and Sergey Zagoruyko. End-to-end object detection with transformers. In *European Conference on Computer Vision*, pages 213–229. Springer, 2020. 2, 3, 4

[5] Kai Chen, Jiangmiao Pang, Jiaqi Wang, Yu Xiong, Xiaoxiao Li, Shuyang Sun, Wansen Feng, Ziwei Liu, Jianping Shi, Wanli Ouyang, et al. Hybrid task cascade for instance segmentation. In *IEEE Conference on Computer Vision and Pattern Recognition*, pages 4974–4983, 2019. 6

[6] Kai Chen, Jiaqi Wang, Jiangmiao Pang, and *et al.* MMDetection: Open mmlab detection toolbox and benchmark. *CoRR*, abs/arXiv:1906.07155, 2019. 5

[7] Gong Cheng, Jiabao Wang, Ke Li, Xingxing Xie, Chunbo Lang, Yanqing Yao, and Junwei Han. Anchor-free oriented proposal generator for object detection. *IEEE Transactions on Geoscience and Remote Sensing*, 60:1–11, 2022. 1, 5, 6

[8] Luc Courtrai, Minh-Tan Pham, and Sébastien Lefèvre. Small object detection in remote sensing images based on super-resolution with auxiliary generative adversarial networks. *Remote Sensing*, 12(19):3152, 2020. 3

[9] Jifeng Dai, Haozhi Qi, Yuwen Xiong, Yi Li, Guodong Zhang, Han Hu, and Yichen Wei. Deformable convolutional networks. In *IEEE Conference on Computer Vision and Pattern Recognition*, pages 764–773, 2017. 4, 7

[10] Jian Ding, Nan Xue, Yang Long, Gui-Song Xia, and Qikai Lu. Learning roi transformer for detecting oriented objects in aerial images. In *IEEE Conference on Computer Vision and Pattern Recognition*, pages 2849–2858, 2019. 1, 2, 3, 6

[11] Jian Ding, Nan Xue, Gui-Song Xia, Xiang Bai, Wen Yang, Michael Ying Yang, Serge Belongie, Jiebo Luo, Mihai Datcu, Marcello Pelillo, et al. Object detection in aerial images: A large-scale benchmark and challenges. *IEEE Transactions on Pattern Analysis and Machine Intelligence*, 44(11):7778–7796, 2021. 1, 5, 6

[12] Dawei Du, Pengfei Zhu, Longyin Wen, and et al. Visdronedet2019: The vision meets drone object detection in image challenge results. In *IEEE International Conference on Computer Vision Workshops*, pages 213–226, 2019. 5, 6

[13] Dominik Maria Endres and Johannes E Schindelin. A new metric for probability distributions. *IEEE Transactions on Information Theory (TIT)*, 49(7):1858–1860, 2003. 4

[14] Zheng Ge, Songtao Liu, Zeming Li, Osamu Yoshie, and Jian Sun. Ota: Optimal transport assignment for object detection. *IEEE Conference on Computer Vision and Pattern Recognition*, 2021. 3, 4, 5

[15] Spyros Gidaris and Nikos Komodakis. Object detection via a multi-region and semantic segmentation-aware cnn model. In *IEEE Conference on Computer Vision and Pattern Recognition*, pages 1134–1142, 2015. 3

[16] Zonghao Guo, Chang Liu, Xiaosong Zhang, Jianbin Jiao, Xiangyang Ji, and Qixiang Ye. Beyond bounding-box: Convex-hull feature adaptation for oriented and densely packed object detection. In *Proceedings of the IEEE/CVF Conference on Computer Vision and Pattern Recognition*, pages 8792–8801, 2021. 5, 6

[17] Jiaming Han, Jian Ding, Jie Li, and Gui-Song Xia. Align deep features for oriented object detection. *IEEE Transactions on Geoscience and Remote Sensing*, 60:1–11, 2021. 1, 3, 5, 6, 8

[18] Jiaming Han, Jian Ding, Nan Xue, and Gui-Song Xia. Redet: A rotation-equivariant detector for aerial object detection. In *IEEE Conference on Computer Vision and Pattern Recognition*, pages 2786–2795, 2021. 1, 6

[19] Kaiming He, Georgia Gkioxari, Piotr Dollar, and Ross Girshick. Mask R-CNN. In *IEEE International Conference on Computer Vision*, pages 2961–2969, 2017. 6

[20] Kaiming He, Xiangyu Zhang, Shaoqing Ren, and Jian Sun. Deep residual learning for image recognition. In *IEEE Conference on Computer Vision and Pattern Recognition*, pages 770–778, 2016. 5

[21] Liping Hou, Ke Lu, Jian Xue, and Yuqiu Li. Shape-adaptive selection and measurement for oriented object detection. In *AAAI Conference on Artificial Intelligence*, 2022. 2, 3, 5, 6

[22] Han Hu, Jiayuan Gu, Zheng Zhang, Jifeng Dai, and Yichen Wei. Relation networks for object detection. In *IEEE Conference on Computer Vision and Pattern Recognition*, pages 3588–3597, 2018. 3

[23] Zhanchao Huang, Wei Li, Xiang-Gen Xia, and Ran Tao. A general gaussian heatmap label assignment for arbitrary-oriented object detection. *IEEE Transactions on Image Processing*, 31:1895–1910, 2022. 2, 3, 4, 5, 6

[24] Kang Kim and Hee Seok Lee. Probabilistic anchor assignment with iou prediction for object detection. In *European Conference on Computer Vision*, pages 355–371. Springer, 2020. 3

[25] Jianan Li, Xiaodan Liang, Yunchao Wei, Tingfa Xu, Jiashi Feng, and Shuicheng Yan. Perceptual generative adversarial networks for small object detection. In *IEEE Conference on Computer Vision and Pattern Recognition*, pages 1222–1230, 2017. 3

[26] Wentong Li, Yijie Chen, Kaixuan Hu, and Jianke Zhu. Oriented reppoints for aerial object detection. In *IEEE Conference on Computer Vision and Pattern Recognition*, pages 1829–1838, 2022. 2, 3, 5, 6

[27] Yanghao Li, Yuntao Chen, Naiyan Wang, and Zhaoxiang Zhang. Scale-aware trident networks for object detection. In *IEEE International Conference on Computer Vision*, pages 6054–6063, 2019. 3

[28] Zhonghua Li, Biao Hou, Zitong Wu, Licheng Jiao, Bo Ren, and Chen Yang. Fcosr: A simple anchor-free rotated detector for aerial object detection. *arXiv preprint arXiv:2111.10780*, 2021. 3

[29] Tsung-Yi Lin, Piotr Dollar, Ross Girshick, Kaiming He, Bharath Hariharan, and Serge Belongie. Feature pyramid networks for object detection. In *IEEE Conference on Computer Vision and Pattern Recognition*, pages 2117–2125, 2017. 3, 5

[30] Tsung-Yi Lin, Priya Goyal, Ross Girshick, Kaiming He, and Piotr Dollar. Focal loss for dense object detection. In *IEEE International Conference on Computer Vision*, pages 2980–2988, 2017. 1, 2, 3, 4, 5, 6, 7, 8

[31] Tsung-Yi Lin, Michael Maire, Serge Belongie, James Hays, Pietro Perona, Deva Ramanan, Piotr Dollár, and C Lawrence Zitnick. Microsoft coco: Common objects in context. In *European Conference on Computer Vision*, pages 740–755. Springer, 2014. 5, 6

[32] Shilong Liu, Feng Li, Hao Zhang, Xiao Yang, Xianbiao Qi, Hang Su, Jun Zhu, and Lei Zhang. Dab-detr: Dynamic anchor boxes are better queries for detr. In *International Conference on Learning Representations*, 2021. 2, 4

[33] Shu Liu, Lu Qi, Haifang Qin, Jianping Shi, and Jiaya Jia. Path aggregation network for instance segmentation. In *IEEE Conference on Computer Vision and Pattern Recognition*, pages 8759–8768, 2018. 3

[34] Wei Liu, Dragomir Anguelov, Dumitru Erhan, Christian Szegedy, Scott Reed, Cheng-Yang Fu, and Alexander C Berg. SSD: Single shot multibox detector. In *European Conference on Computer Vision*, pages 21–37. Springer, 2016. 3

[35] Zikun Liu, Hongzhen Wang, Lubin Weng, and Yiping Yang. Ship rotated bounding box space for ship extraction from high-resolution optical satellite images with complex backgrounds. *IEEE Geoscience and Remote Sensing Letters*, 13(8):1074–1078, 2016. 1

[36] Jianqi Ma, Weiyuan Shao, Hao Ye, Li Wang, Hong Wang, Yingbin Zheng, and Xiangyang Xue. Arbitrary-oriented scene text detection via rotation proposals. *IEEE Transactions on Multimedia*, 20(11):3111–3122, 2018. 1, 2

[37] Yuchen Ma, Songtao Liu, Zeming Li, and Jian Sun. Iqdet: Instance-wise quality distribution sampling for object detection. In *Proceedings of the IEEE/CVF Conference on Computer Vision and Pattern Recognition*, pages 1717–1725, 2021. 3

[38] Qi Ming, Zhiqiang Zhou, Lingjuan Miao, Hongwei Zhang, and Linhao Li. Dynamic anchor learning for arbitrary-oriented object detection. In *AAAI Conference on Artificial Intelligence*, volume 35, pages 2355–2363, 2021. 2, 3, 5, 6

[39] Frank Nielsen. On a generalization of the jensen–shannon divergence and the jensen–shannon centroid. *Entropy*, 22(2):221, 2020. 2, 4, 7

[40] Junhyug Noh, Wonho Bae, Wonhee Lee, Jinhwan Seo, and Gunhee Kim. Better to follow, follow to be better: Towards precise supervision of feature super-resolution for small object detection. In *IEEE International Conference on Computer Vision*, pages 9725–9734, 2019. 3

[41] Adam Paszke, Sam Gross, Francisco Massa, Adam Lerer, et al. Pytorch: An imperative style, high-performance deep learning library. In *Advances in Neural Information Processing Systems*, pages 8024–8035, 2019. 5

[42] Siyuan Qiao, Liang-Chieh Chen, and Alan Yuille. Detectors: Detecting objects with recursive feature pyramid and switchable atrous convolution. In *IEEE Conference on Computer Vision and Pattern Recognition*, 2021. 3

[43] Jakaria Rabbi, Nilanjan Ray, Matthias Schubert, Subir Chowdhury, and Dennis Chao. Small-object detection in remote sensing images with end-to-end edge-enhanced gan and object detector network. *Remote Sensing*, 12(9):1432, 2020. 3

[44] Shaoqing Ren, Kaiming He, Ross Girshick, and Jian Sun. Faster R-CNN: Towards real-time object detection with region proposal networks. In *Advances in Neural Information Processing Systems*, pages 91–99, 2015. 1, 2, 6

[45] Olga Russakovsky, Jia Deng, Hao Su, Jonathan Krause, Sanjeev Satheesh, Sean Ma, Zhiheng Huang, Andrej Karpathy, Aditya Khosla, Michael Bernstein, et al. Imagenet large scale visual recognition challenge. *International Journal of Computer Vision*, 115(3):211–252, 2015. 5

[46] Bharat Singh and Larry S Davis. An analysis of scale invariance in object detection snip. In *IEEE Conference on Computer Vision and Pattern Recognition*, pages 3578–3587, 2018. 3

[47] Bharat Singh, Mahyar Najibi, and Larry S Davis. Sniper: Efficient multi-scale training. In *Advances in Neural Information Processing Systems*, pages 9310–9320, 2018. 3

[48] Peize Sun, Rufeng Zhang, Yi Jiang, Tao Kong, Chenfeng Xu, Wei Zhan, Masayoshi Tomizuka, Lei Li, Zehuan Yuan, Changhu Wang, and Ping Luo. Sparse r-cnn: End-to-end object detection with learnable proposals. In *IEEE Conference on Computer Vision and Pattern Recognition*, pages 14454–14463, 2021. 2, 4

[49] Mingxing Tan, Ruoming Pang, and Quoc V Le. Efficientdet: Scalable and efficient object detection. In *IEEE Conference on Computer Vision and Pattern Recognition*, pages 10781–10790, 2020. 3

[50] Zhi Tian, Chunhua Shen, Hao Chen, and Tong He. FCOS: Fully convolutional one-stage object detection. In *IEEE International Conference on Computer Vision*, pages 9627–9636, 2019. 1, 5

[51] Zhi Tian, Chunhua Shen, Hao Chen, and Tong He. Fcos: A simple and strong anchor-free object detector. *IEEE Transactions on Pattern Analysis and Machine Intelligence*, 2020. 6

[52] Jiaqi Wang, Kai Chen, Shuo Yang, Chen Change Loy, and Dahua Lin. Region proposal by guided anchoring. In *IEEE Conference on Computer Vision and Pattern Recognition*, pages 2965–2974, 2019. 8

[53] Jinwang Wang, Wen Yang, Heng-chao Li, Haijian Zhang, and Gui-Song Xia. Learning center probability map for detecting objects in aerial images. *IEEE Transactions on Geoscience and Remote Sensing*, 59(5):4307–4323, 2021. 5

[54] Yingming Wang, Xiangyu Zhang, Tong Yang, and Jian Sun. Anchor detr: Query design for transformer-based detector. In *AAAI Conference on Artificial Intelligence*, volume 36, pages 2567–2575, 2022. 2, 3

[55] Gui-Song Xia, Xiang Bai, Jian Ding, Zhen Zhu, Serge Belongie, Jiebo Luo, Mihai Datcu, Marcello Pelillo, and Liangpei Zhang. DOTA: A large-scale dataset for object detection in aerial images. In *IEEE Conference on Computer Vision and Pattern Recognition*, pages 3974–3983, 2018. 1, 5, 6

[56] Xingxing Xie, Gong Cheng, Jiabao Wang, Xiwen Yao, and Junwei Han. Oriented r-cnn for object detection. In *IEEE International Conference on Computer Vision*, pages 3520–3529, 2021. 2, 6

[57] Chang Xu, Jinwang Wang, Wen Yang, Huai Yu, Lei Yu, and Gui-Song Xia. Detecting tiny objects in aerial images: A normalized wasserstein distance and a new benchmark. In *ISPRS Journal of Photogrammetry and Remote Sensing*, volume 190, pages 79–93, 2022. 3

[58] Chang Xu, Jinwang Wang, Wen Yang, Huai Yu, Lei Yu, and Gui-Song Xia. Rfla: Gaussian receptive field based label assignment for tiny object detection. In *European Conference on Computer Vision*, pages 526–543. Springer, 2022. 3, 4, 6

[59] Chang Xu, Jinwang Wang, Wen Yang, and Lei Yu. Dot distance for tiny object detection in aerial images. In *IEEE Conference on Computer Vision and Pattern Recognition Workshops*, pages 1192–1201, 2021. 2

[60] Xue Yang, Qingqing Liu, Junchi Yan, Ang Li, Zhiqiang Zhang, and Gang Yu. R3det: Refined single-stage detector with feature refinement for rotating object. *CoRR*, abs/arXiv:1908.05612, 2019. 1, 3, 5, 6, 8

[61] Xue Yang, Junchi Yan, Qi Ming, Wentao Wang, Xiaopeng Zhang, and Qi Tian. Rethinking rotated object detection with gaussian wasserstein distance loss. In *International Conference on Machine Learning*, volume 139, pages 11830–11841, 2021. 4, 7

[62] Xue Yang, Jirui Yang, Junchi Yan, Yue Zhang, Tengfei Zhang, Zhi Guo, Xian Sun, and Kun Fu. SCRDet: Towards more robust detection for small, cluttered and rotated objects. In *IEEE International Conference on Computer Vision*, pages 8232–8241, 2019. 1

[63] Xue Yang, Xiaojiang Yang, Jirui Yang, Qi Ming, Wentao Wang, Qi Tian, and Junchi Yan. Learning high-precision bounding box for rotated object detection via kullback-leibler divergence. *Advances in Neural Information Processing Systems*, 34, 2021. 4, 5, 6, 7

[64] Xue Yang, Gefan Zhang, Xiaojiang Yang, Yue Zhou, Wentao Wang, Jin Tang, Tao He, and Junchi Yan. Detecting rotated objects as gaussian distributions and its 3-d generalization. *IEEE Transactions on Pattern Analysis and Machine Intelligence*, 2022. 4, 5

[65] Ze Yang, Shaohui Liu, Han Hu, Liwei Wang, and Stephen Lin. Reppoints: Point set representation for object detection. In *IEEE International Conference on Computer Vision*, pages 9657–9666, 2019. 3

[66] Jiahui Yu, Yuning Jiang, Zhangyang Wang, Zhimin Cao, and Thomas Huang. Unitbox: An advanced object detection network. pages 516–520, 2016. 5

[67] Mohsen Zand, Ali Etemad, and Michael Greenspan. Objectbox: From centers to boxes for anchor-free object detection. *European Conference on Computer Vision*, 2022. 4, 7

[68] Shifeng Zhang, Cheng Chi, Yongqiang Yao, Zhen Lei, and Stan Z Li. Bridging the gap between anchor-based and anchor-free detection via adaptive training sample selection. In *IEEE Conference on Computer Vision and Pattern Recognition*, pages 9759–9768, 2020. 1, 2, 3, 4, 5, 6

[69] Qijie Zhao, Tao Sheng, Yongtao Wang, Zhi Tang, Ying Chen, Ling Cai, and Haibin Ling. M2det: A single-shot object detector based on multi-level feature pyramid network. In *AAAI Conference on Artificial Intelligence*, pages 9259–9266, 2019. 3

[70] Yue Zhou, Xue Yang, Gefan Zhang, Jiabao Wang, Yanyi Liu, Liping Hou, Xue Jiang, Xingzhao Liu, Junchi Yan, Chengqi Lyu, et al. Mmrotate: A rotated object detection benchmark using pytorch. *arXiv preprint arXiv:2204.13317*, 2022. 5, 6

[71] Chenchen Zhu, Yihui He, and Marios Savvides. Feature selective anchor-free module for single-shot object detection. In *IEEE Conference on Computer Vision and Pattern Recognition*, pages 840–849, 2019. 4

[72] Xizhou Zhu, Weijie Su, Lewei Lu, Bin Li, Xiaogang Wang, and Jifeng Dai. Deformable detr: Deformable transformers for end-to-end object detection. In *International Conference on Learning Representations*, 2021. 3